Potential serpentinization, degassing, and gas hydrate formation at a young (<20 Ma) sedimented ocean crust of the Arctic Ocean ridge system

Anupama Rajan,[1] Jürgen Mienert,[1] Stefan Bünz,[1] and Shyam Chand[2]

Received 19 May 2011; revised 21 December 2011; accepted 9 January 2012; published 9 March 2012.

[1] Global assessment of methane must consider the role of mid-ocean ridges. Fluids from serpentinized mantle and gabbro material are noteworthy on ocean ridges, although they are not very well understood. Only a few sedimented ocean ridges exist worldwide, and they may document past and ongoing serpentinization-driven migration of gas-rich fluids. This study is based on two multichannel reflection seismic profiles acquired across a sedimented segment of the ultraslow spreading Knipovich Ridge offshore NW Svalbard. Seismic data allow suggesting a potential link between inferred areas of serpentinization, transfer of carbon from the deep-seated host rocks through the sediments above by diapirism, and methane capture within the gas hydrate stability zone at the eastern flank of the Knipovich Ridge. The origin of sediment remobilization features can be related to intrusions and the degassing process from mantle serpentinization. These disturbances in sediments overlying the oceanic crust can be observed in seismic data and are interpreted as diapirs. In shallower sediments, at the predicted base of the gas hydrate stability zone, the seismic data show a bright spot with all the characteristics of a gas hydrate related bottom-simulating reflector (BSR), such as enhanced reflection amplitude, phase reversal relative to the seabed reflection, and crosscutting of sedimentary strata. The BSR occurs at about 200 ms two-way time within a sequence of marine sediments. Two-dimensional concentration models of methane hydrate using the differential effective medium theory predict saturations of up to 26% of methane hydrate in the pore space of sediments in the gas hydrate reservoir.

Citation: Rajan, A., J. Mienert, S. Bünz, and S. Chand (2012), Potential serpentinization, degassing, and gas hydrate formation at a young (<20 Ma) sedimented ocean crust of the Arctic Ocean ridge system, *J. Geophys. Res.*, *117*, B03102, doi:10.1029/2011JB008537.

1. Introduction

[2] Fluid-rock interaction between the crust, mantle, and oceans can cause serpentinization processes [*Kelley and Früh-Green*, 1999; *Früh-Green et al.*, 2003; *Kelley et al.*, 2005; *Vance et al.*, 2007; *Proskurowski et al.*, 2008]. In recent years, studies at mid-ocean ridge systems have detected the presence of elevated concentrations of methane from the host rocks to the circulating fluid or through magmatic degassing that are undergoing serpentinization reactions [*Kelley and Früh-Green*, 1999; *Proskurowski et al.*, 2008]. These discoveries demonstrated that the abiotic synthesis of hydrogen and hydrocarbons may occur in deep-sea environments in the presence of ultramafic rocks, water, and moderate amounts of heat by Fischer-Tropsch-type (FTT) reactions [*Proskurowski et al.*, 2008]. As a consequence of the formation of magnetite, hydrogen gas (H_2) is produced from the reduction of seawater during serpentinization. Seawater also contains carbonate and sulfate ions which can become reduced to form methane (CH_4) and hydrogen sulfide (H_2S) during the serpentinization process. The presence of H_2, CH_4 and H_2S in fluids that seep out of the rocks provide important energy sources for different microbial species found at hydrothermal vents [*Sleep et al.*, 2004; *Judd and Hovland*, 2007; *Proskurowski et al.*, 2008].

[3] Methane derived from magma-driven thermogenic alteration of sediments has been recently reported from a young sedimented ocean spreading center [*Lizarralde et al.*, 2011]. Here individual gas accumulations comprise complex and dynamic systems in which gas feeds seafloor biogenic communities. In continental margins new gas is normally generated at shallow depth by bacteria and at much greater depth by thermal cracking of organic material [e.g., *Claypool and Kvenvolden*, 1983]. As dissolved gas migrates upward and forms gas bubbles the pore waters may become saturated, and eventually may form gas hydrate within the gas hydrate stability zone (GHSZ) [*Sloan*, 1998]. In most of these cases, the dominant gas in the solid phase is methane, produced by the bacterial decomposition of organic matter in deep-sea sediments [*Judd et al.*, 2002]. The deposition of

[1]Department of Geology, University of Tromsø, Tromsø, Norway.
[2]Geological Survey of Norway, Trondheim, Norway.

0148-0227/12/2011JB008537

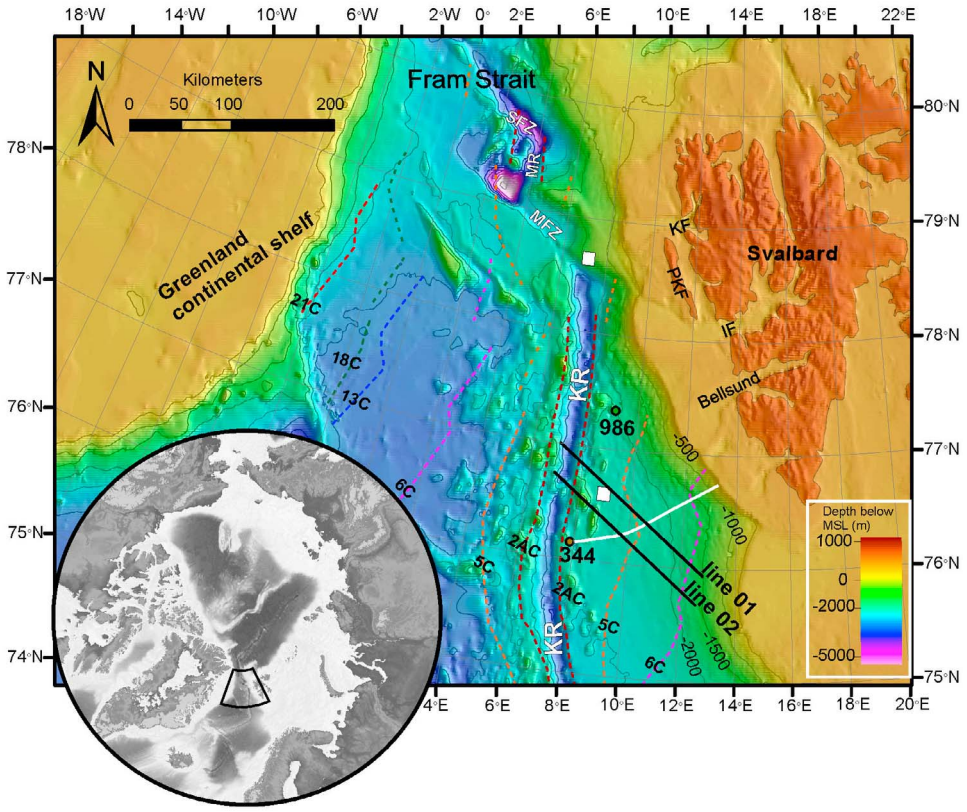

Figure 1. Bathymetry (IBCAO) [*Jakobsson et al.*, 2000] map with the main structural features of the western Svalbard margin and the mid-ocean ridge systems. Lines 01 and 02 are the seismic profiles presented in this paper. The same profiles were used by *Kandilarov et al.* [2008]. The small white square boxes are the Hydratech survey areas [*Mienert et al.*, 2001; *Vanneste et al.*, 2005b, *Westbrook et al.*, 2008]. The white seismic line [*Eiken and Hinz*, 1993] connects DSDP Site 344 with multichannel seismic (MCS) lines 01 and 02. Green and yellow circles represent ODP 986 and DSDP 344 drill holes, respectively. Magnetic anomalies 5C (9.8 Ma) and 6C (19.6 Ma) illustrate the young subsedimentary oceanic crust offshore west Svalbard [from *Engen et al.*, 2008]. SFZ, Spitsbergen Fracture Zone; MR, Molloy Ridge; MFZ, Molloy Fracture Zone; KR, Knipovich Ridge; KF, Kongsfjorden; IF, Isfjorden; PKF, Prins Karls Forland.

sediment over time slowly brings the gas hydrate to higher-temperature regions with increasing depth. At higher temperature (>20°C), gas hydrate is no longer stable and dissociates so that gas-saturated water including gas bubbles may ascend. While much of the gas from deep areas is retrapped in the GHSZ after migrating into cooler and shallower zones, some gas escapes through the seafloor into the ocean [e.g., *Hustoft et al.*, 2009; *Westbrook et al.*, 2009].

[4] Gas hydrates are crystalline water-based solids physically resembling ice that are stable at high pressure and low temperature when gas concentration exceeds the solubility limit [*Sloan*, 1998]. Gas hydrates have been found to occur naturally in large quantities and are widely present in continental margins [*Kvenvolden*, 1988] where the deep water column provides enough pressure to stabilize gas hydrate. The base of the GHSZ (BGHSZ) is mostly inferred from the presence of a bottom-simulating reflector (BSR) on reflection seismic data [*Shipley et al.*, 1979]. The BSR represents a contrast in acoustic impedance due to free gas accumulating beneath a more impermeable gas hydrate zone. The BSR can usually be identified on seismic data because it mimics the seafloor topography and shows opposite seismic polarity with respect to the seafloor [*Markl et al.*, 1970; *Shipley et al.*, 1979; *Hyndman and Spence*, 1992]. Since the depths of many BSRs coincide stratigraphically with the pressure and temperature conditions of methane hydrate stability, the BSR has been used to indirectly estimate heat flow [*Yamano et al.*, 1982; *Vanneste et al.*, 2005a]. Gas hydrates may also exist without a BSR as documented by Blake Ridge drilling results [*Holbrook et al.*, 1996; *Holbrook et al.*, 2002]. A detailed knowledge of *P* wave velocity anomaly distributions in marine sediments [e.g., *Hustoft et al.*, 2009] and effective medium theories are used to derive quantitative estimates of gas hydrate and free gas in the pore space of sediments [*Ecker et al.*, 2000; *Jakobsen et al.*, 2000; *Chand et al.*, 2004].

[5] Multichannel (MCS), single channel (SCS), and multicomponent ocean bottom seismic (OBS) data have revealed the presence of gas hydrate and free gas on the western Svalbard margin (Figure 1) [*Eiken and Hinz*, 1993; *Posewang and Mienert*, 1999; *Vanneste et al.*, 2005b; *Westbrook et al.*, 2008; *Hustoft et al.*, 2009]. These results demonstrated that free gas, gas hydrates and enhanced

reflections are prominent features east of this ocean spreading center (Figure 1).

[6] This study concentrates on the northern Knipovich Ridge with the aim to shed more light on the potential link between suggested areas of serpentinization, upward fluid migration and methane capture in gas hydrates on a sedimented ocean ridge. Two MCS lines crossing the oceanic ridge are used: MCS line 01 crossing a part of ridge with less relief and MCS line 02, an area with significant relief. The MCS data allowed determining regions of diapiric structures and bright spots on top of oceanic crustal highs while compressional wave velocity modeling was the base for determining and estimating the concentration of methane hydrate using the partial hydrate cementing model [*Chand et al.*, 2006].

2. Geological Setting

[7] For the last several decades the Knipovich Ridge and the neighboring Svalbard continental margin (Figure 1) at the Fram Strait have been extensively studied using reflection and refraction seismic data as well as seismological, bathymetric, gravity, magnetic, thermal, geochemical and well data [*Sundvor and Eldholm*, 1979; *Myhre*, 1984; *Crane et al.*, 1991; *Faleide et al.*, 1996; *Fiedler and Faleide*, 1996: *Hjelstuen et al.*, 1996; *Crane et al.*, 2001; *Lundin and Doré*, 2002; *Mosar et al.*, 2002; *Okino et al.*, 2002; *Ritzmann et al.*, 2002; *Engen et al.*, 2003; *Ljones et al.*, 2004; *Ritzmann et al.*, 2004; *Engen et al.*, 2008; *Sarkar et al.*, 2011]. The Knipovich Ridge shows a prominent central rift valley (Figure 1). The relief of the eastern flank of the ridge facing the west Svalbard continental margin is almost completely buried by sediments [*Talwani and Eldholm*, 1977]. In contrast, the topographic relief of the western flank is much more prominent because of the lack of sediment supply from the (~300 km) far away east Greenland continental margin. Opening of the Norwegian-Greenland Sea started in the early Eocene [*Engen et al.*, 2008] with a change in plate configuration and spreading direction in earliest Oligocene (35 Ma). Changes of plate movement in the Oligocene resulted in the development and activation of the Knipovich Ridge forcing continental separation of Greenland and Svalbard [*Lundin and Doré*, 2002]. The opening of the northern Norwegian-Greenland Sea caused the Knipovich Ridge to propagate from the south into the Spitsbergen Shear zone [*Crane et al.*, 1988]. After subsidence, the Fram Strait developed as the only deep water passage to the Arctic Ocean, playing a key role in Atlantic-Arctic ocean circulation processes [*Eiken and Hinz*, 1993].

[8] The Knipovich Ridge is a part of the Arctic Ocean ridge system connected to the Nansen-Gakkel Ridge in the eastern Arctic. The spreading rate along the Knipovich Ridge varies from a maximum of 18 mm/yr in the south to 12.7 mm/yr in the north [*Dick et al.*, 2003]. The Knipovich Ridge extends from the Mohns Ridge in the south at ~73°50′N to the Molloy Fracture zone in the north at ~78°30′N. It is about 550 km long with spreading direction oblique to the rift and varying along the ridge, from 41° to 55° [*Dick et al.*, 2003]. The spreading is highly asymmetric, with a spreading rate of 7 mm/yr to the west and 1 mm/yr to the east [*Myhre et al.*, 1982; *Crane et al.*, 1991, 2001; *Dick et al.*, 2003; *Engen et al.*, 2003; *Ljones et al.*, 2004; *Kandilarov et al.*, 2008]. On the basis of the spreading rate of the Knipovich Ridge it has been classified as transitional between slow and ultraslow spreading [*Dick et al.*, 2003]. However, because of the poorly developed magnetic anomalies [*Engen et al.*, 2008] spreading rate and age constraints are somewhat uncertain. Noteworthy is that the whole Knipovich Ridge at its western flank appears to be more elevated than the eastern flank [*Crane et al.*, 2001; *Engen et al.*, 2003]. This has been explained by the fact that the Svalbard archipelago and the Barents Sea shelf fed considerable amount of sediments into the area, which have been effectively fenced by the ridge, so that a large mass of sediments has accumulated east of the ridge while almost no sediments have been deposited west of it. Because of high sediment loading, the eastern flank has subsided several hundred meters relative to the western flank [*Faleide et al.*, 1996; *Fiedler and Faleide*, 1996; *Hjelstuen et al.*, 1996; *Crane et al.*, 2001; *Engen et al.*, 2003; *Kandilarov et al.*, 2008].

[9] Three sedimentary depositional sequences are identified offshore central Spitsbergen [*Schlüter and Hinz*, 1978], SPI-I, SPI-II, and SPI-III, which are separated by two unconformities, U1 and U2. The preglacial strata, G0 corresponds to SPI-III. The late Cenozoic glacial sediments comprising three main sequences, GI, GII and GIII relate to SPI-II and SPI-I, the two main units of the Cenozoic succession [*Fiedler and Faleide*, 1996; *Sarkar et al.*, 2011]. According to *Myhre and Eldholm* [1988] and *Schlüter and Hinz* [1978], the chaotic character observed in SPI-II, which is clearly different from the stratified sequences SPI-I and SPI-III, is a result from downslope mass movements. *Eiken and Austegard* [1987] related some of the features to mud diapirism and *Eiken and Hinz* [1993] identified also contourite deposits in this area.

[10] The SPI-I sequence consists of Plio-Pleistocene glaciomarine sediments and turbidites with average compressional wave velocities from 1.7 to 2.8 km/s [*Schlüter and Hinz*, 1978]. SPI-II consists of Pliocene sediments with velocities from 2.4 to 2.8 km/s. The underlying unconformity U1 and SPI-III sequence of pre–middle Oligocene age shows velocities from 2.9 to 4.8 km/s with a distinct unconformity (U2) at its base. *Myhre and Eldholm* [1988] revealed that the glaciomarine sediments in the SPI-I sequence over spilled the Knipovich Ridge axial valley.

3. Data and Methods

3.1. Multichannel Seismic Data

[11] Two MCS profiles (acquired during a R/V Håkon Mosby cruise in September 2002 by the University of Bergen) run parallel to the spreading direction on the eastern flank of the Knipovich Ridge (Figure 1). The seismic data were recorded using a 3000 m long, 240 channel digital streamer with 12.5 m receiver group interval. The survey was acquired with a shot interval of 50 m, a streamer depth of 10 m, a record length of 12 s and a sampling rate of 2 ms. The group interval of 12.5 m provides a common midpoint (CMP) spacing of 6.25 m. The seismic source consisted of an air gun array consisting of 5 air guns each with a volume of 60, 90, 136, 210, and 340 $inch^3$ and one additional 580 $inch^3$ gun operated at a tow depth of 7 m depth. The streamer recording was done with a 3 Hz low-cut filter and a

180 Hz high-cut filter with slopes of 18 and 72 dB/octave, respectively.

3.2. MCS Processing and Velocity Analysis

[12] Processing of MCS data allowed multiple attenuation and enhancing the basement reflector. Standard processing [*Yilmaz*, 1987] was applied to the MCS profiles line 01 and line 02 with band-pass filtering 5–10–100–120 Hz on shot gathers to remove low-frequency noise (this frequency also has least influence on the primary reflection). Furthermore, we applied CMP sorting, velocity analysis, amplitude gain, normal moveout (NMO) correction, dip moveout correction, stacking, predictive deconvolution and Stolt F-K migration. We used a forward NMO correction and DMO correction followed by inverse NMO and pre stack time migration in the FK domain [*Stolt*, 1978] using NMO velocities. A velocity analysis along the profiles was conducted including detailed velocity analysis between CMPs 11700–13500 (for line 01) and CMPs 11200–16500 and 17400–21500 (for line 02). CMP gathers at intervals of 25CMPs were selected for velocity analysis. The velocity analysis was based on the analysis of stacking velocities on the prestack data to obtain root-mean-square (RMS) velocities, and convert RMS velocities into physical interval velocities using *Dix*'s [1955] equation. The picked velocities were subsequently used during stacking of DMO corrected CMP gathers.

[13] The semblance peak width and the picked stacked velocities can be related to the interval velocity uncertainties. The interpretation of the data set has been very precise because we concentrated on the highly variable and heterogeneous nature of the velocities and structural elements pertaining to the ridge in the study area. The submarine region with the sedimentary strata that overlies the oceanic basement appears to be well defined with negligible distortions in the time sections.

[14] The errors included while picking the stacking velocities have a direct bearing on the uncertainty of the interval velocities. On the basis of the width of the semblance peak of the processed seismic data sets, a maximum picking error of ± 5 m/s is estimated. This variation in RMS velocity can result in an error in the range of 50–150 m/s in the interval velocity. As in the case with stacking velocities, there is a tradeoff between adjacent layers separated by a horizon that is defined by the velocity pick. If velocity increases in one of the two layers, then velocity decreases in the other. In case of the reflection at the BGHSZ, it can either enhance velocity anomalies in the hydrate and gas bearing zone or it can suppress them [*Bünz and Mienert*, 2004]. However, as the velocities were determined frequently and rigorously along the lines in the data set, the picking errors have been nullified by the smoothing operation and as a result we anticipate the error in interval velocity to be much less than 80 m/s.

3.3. Gas Hydrate and Free Gas Modeling Using DEM

[15] *Chand et al.* [2006] introduced an algorithm based on effective medium modeling to infer hydrate saturation from compressional wave velocity and attenuation measurements on hydrate-bearing sediments. This inversion algorithm relates the seismic properties of hydrate-bearing sediments to porosity, mineralogy, microstructure and hydrate saturation. We applied this model to quantify the gas hydrate concentration as this model has been widely utilized for hydrate quantification and proven in different geological settings [*Jakobsen et al.*, 2000; *Chand et al.*, 2004, 2006]. Above the BSR, the hydrate saturation is adjusted to improve the fit between the calculated and observed seismic velocities and the amount of hydrate cementing the grains is linearly increased with an increase in hydrate saturation [*Hustoft et al.*, 2009]. The velocity and attenuation increases with an increase in hydrate saturation, which strengthens the sediment microstructure. The increase in attenuation also relate to the hydrate permeability. We use effective medium inversion algorithm based on the self-consistent approximation (SCA) and differential effective medium (DEM) theory [*Jakobsen et al.*, 2000; *Chand et al.*, 2004].

[16] ODP Site 986 (Leg 162) lies $\sim$77.6 and $\sim$109.9 km to the north of MCS profiles 01 and 02, respectively. A porosity-depth function [*Hustoft et al.*, 2009] is used on the basis of porosity measurements from site 986 [*Forsberg et al.*, 1999; *Shipboard Scientific Party*, 1996]. In order to be consistent, we used the sediment composition for the Svalbard study area obtained from the Hydratech site (Figure 1) and the compositions are given as 53% of clay/mica, 24% quartz, 5% of K feldspar, 11% of plagioclase, 7% of calcite [*Hydratech*, 2004]. The best fit porosity profile [e.g., *Hustoft et al.*, 2009] along with these sediment compositions and sediment rigidity is then used to compute the reference velocity for the gas hydrate prediction.

3.4. BGHSZ Modeling

[17] We modeled the GHSZ in the area using the formula by *Sloan* [1998] modified by *Chand et al.* [2008] for hydrostatic pressure, pore water composition (seawater salinity) and geothermal gradient. The compiled geothermal data from this area in the HEAT database are sparse [*Planke*, 1989]. Heat flow values range from 301 ± 4 mW m^{-2} at the ridge to 50 mW m^{-2} further away from the flanks. Our study area falls close to a heat flow value of 75 mW m^{-2} with an average thermal conductivity of 1.1 W m^{-1} K^{-1} [*Sundvor et al.*, 2000]. Additional parameters used for determining the subbottom depth of hydrate stability are the bathymetry and the bottom water temperature (World Ocean Database, http://www.nodc.noaa.gov/General/temperature.html).

4. Results

4.1. Seismic Reflection Interpretation

[18] The seismic data (Figures 2a and 3a) show well-stratified layers of sedimentary sequences in the upper units from the slope toward the Knipovich Ridge (Figures 2a and 3a). Beneath and intermittently, the stratification is interrupted by rather extensive and chaotic intervals lacking internal structures because of mass movements. The boundary between the upper stratified sedimentary units and the chaotic sequences beneath is particularly obvious between GI and GII. Toward the northwest, i.e., the ridge, the zone undulates and is significantly deformed by dome-like, anticlinal structures (Figures 2 and 3). The anticlinal structures are usually several km wide and cause variably strong deformation of the overlying strata. Their internal reflection characteristic is mostly chaotic (Figures 2 and 3). However, some of the structures show enhanced reflection amplitudes at their rim and also within (Figures 2 and 3). The overall appearance of

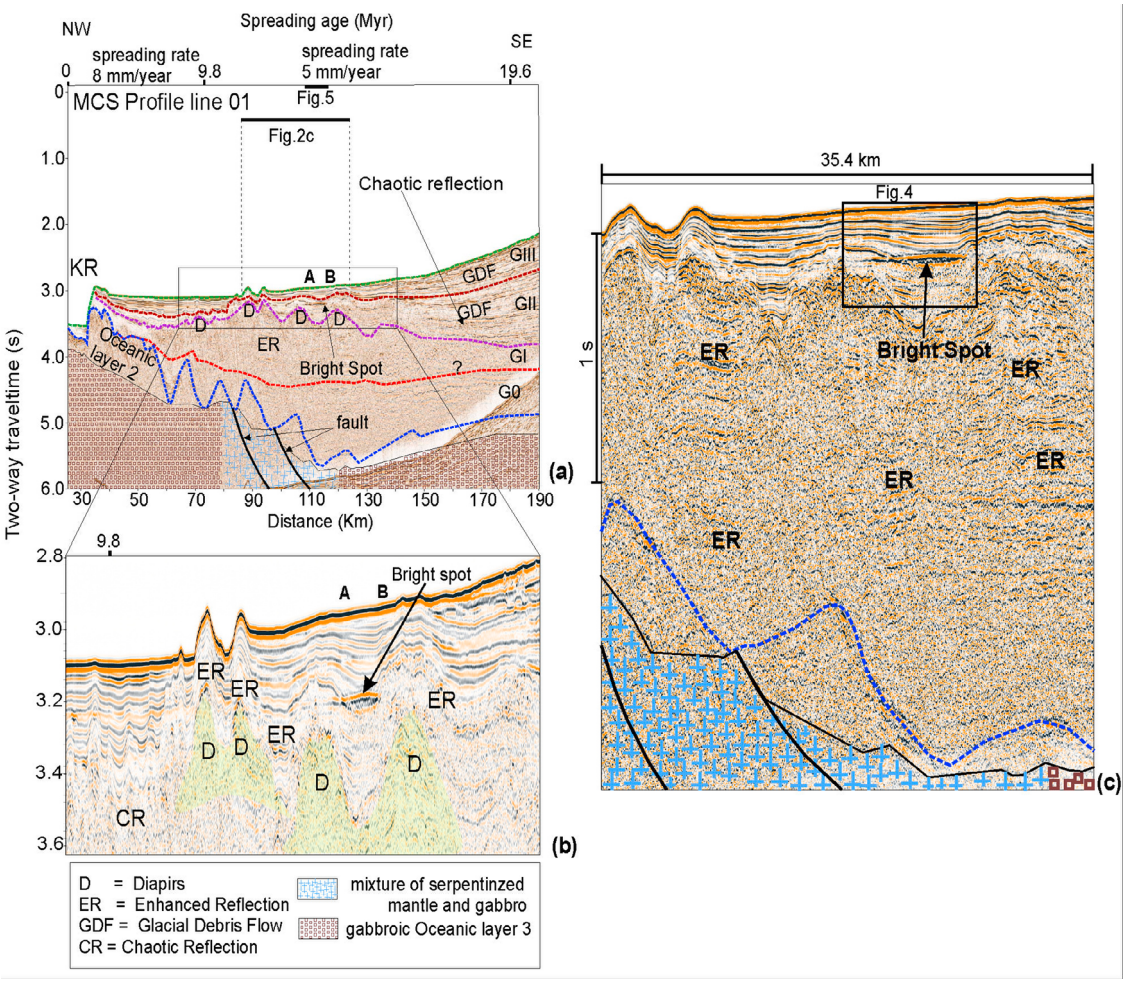

Figure 2. Seismic observations of serpentinization across Knipovich Ridge spreading segment. (a) MCS profiles 01 indicates a bright spot, glacial debris flow deposits (GDF), enhanced reflection, and diapirs with chaotic strata and illustrates the stratigraphic architecture across the SW Svalbard margin from the Knipovich Ridge to the continental slope. The horizons are interpreted as the seabed (green), glacial sequences GIII (dark brown), GII (purple), GI (red), and preglacial sequence G0 (blue) as well as oceanic basement. GI, GII, and GIII are the glacial units of late Cenozoic age. The mixture of serpentinized mantle and gabbro area is extracted from *Kandilarov et al.* [2008]. (b) A bright spot measuring 6 km in length with underlying disturbed strata. (c) Zoomed area of the enhanced reflections beneath the bright spot from seismic profile line 01.

these anticlinal structures suggests that they are diapirs. Some of the diapiric structures cause very pronounced seafloor features while others are buried and sedimentation has flattened out the seafloor (Figures 2 and 3) indicating differences in the amplitudes of vertical diapir movement. In general, sediment deformations become more evident toward the areas where oceanic basement shoals (Figures 2 and 3).

[19] A very pronounced chaotic reflection pattern in the sedimentary sequences extends from the lower slope toward the Knipovich Ridge and occurs over a depth range of at least 2 s TWT (Figures 2a and 3a). The chaotic unit shows several short (<10 km) segments of enhanced reflections occurring almost throughout its entire depth range (Figure 2c). However, the enhanced reflections are confined to the area where the diapirs exist. Together with the close distance between the diapirs, it suggests that the diapirs might have a common root zone. An amagmatic segment, suggested to be composed of a mixture of serpentinized mantle and gabbro [*Kandilarov et al.*, 2008] lies beneath the area with the enhanced reflection amplitude and the diapiric structures (Figure 2).

[20] Seismic profile line 01 (Figure 2) shows a distinct bright spot measuring nearly 6 km in length between two diapiric structures at a distance of ~110 km from the ridge axis (Figures 2a and 2b). The bright spot reflection also crosscuts through the deformed sedimentary strata at about 200 ms TWT in the upper sections of the GII sedimentary sequence (Figure 4). Together, these observations suggest that the bright spot resembles a gas hydrate related BSR. The BSR occurs at the expected theoretical base of the BGHSZ [e.g., *Vanneste et al.*, 2005b]. The BSR is not characterized by a continuous reflection, but instead abruptly terminates (Figures 2 and 4). However, weak crosscutting seismic amplitudes suggest that the BSR continues further northwest

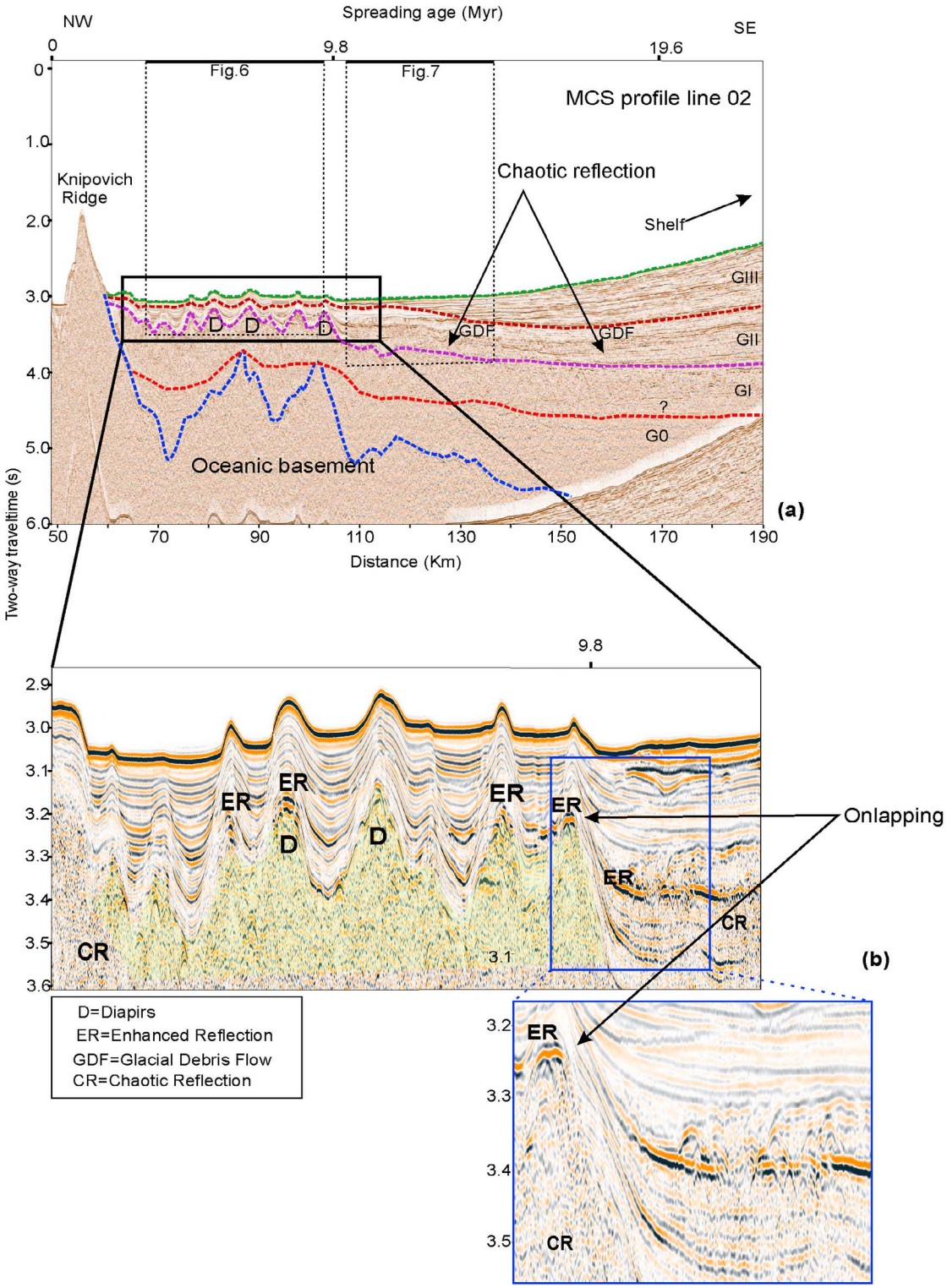

Figure 3. (a) MCS profile 02 runs from the Knipovich Ridge to the continental slope showing glacial debris flow diapirs and depicting oceanic basement highs beneath. The horizons are interpreted as the seabed (green), glacial sequences GIII (dark brown), GII (purple), and GI (red), and preglacial sequence G0 (blue) as well as oceanic basement. GI, GII, and GIII are the glacial units of late Cenozoic age. (b) Diapirs interrupt the stratigraphic architecture at the sedimented Knipovich Ridge, and diapirism influences the seafloor and indicates some onlapping at the rim of the diapirs.

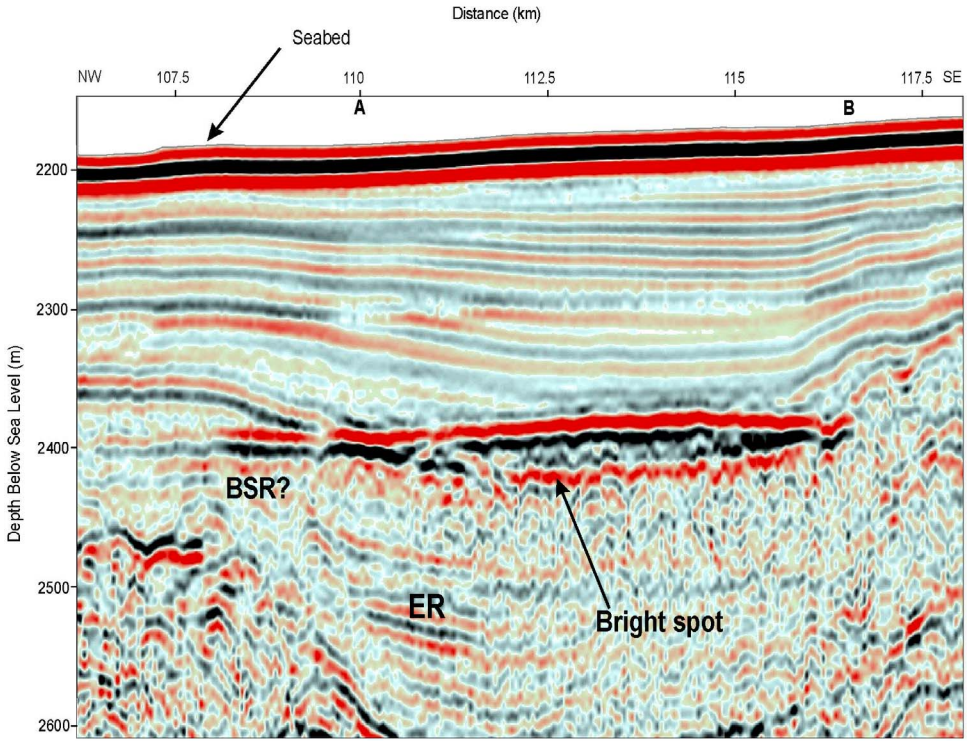

Figure 4. MCS profile line 01 shows a bright spot and enhanced reflection (ER) on top of a basin-like structure with the characteristics of a bottom-simulating reflector (BSR), i.e., negative apparent polarity relative to reflections of the seabed and strata crosscutting seismic events. The area between points A and B shows the extension of the bright spot.

through the diapiric structures and into the next small mini basin that forms between diapirs (Figures 2b and 2c). Directly below the BSR and beneath the BGHSZ, the area is marked by interrupted and faint reflections, possibly because seismic energy has been scattered and attenuated by gassy sediments underlying the gas hydrate–free gas boundary (Figure 2).

[21] Seismic profile line 02 encompasses the oceanic basement and above the preglacial sequence G0 and on top glacial sequences GIII to GI (Figure 3a). The identified sequences GIII and GII generally show continuous seismic reflections that are distinguished from the lower sequence GI and G0 with more disturbed seismic patterns (Figure 3a).

[22] The GIII sequence resembles a basin fill with well stratified layers extending from the continental slope at 190 km away from the ridge to the eastern flank of the Knipovich Ridge at ~60 km (Figure 3a). At various places between ~60 km and ~110 km, the sediment thickness is reduced because of the underlying diapir structures of the GI sequence and oceanic basement morphology (Figure 3a). Enhanced reflection (ER) amplitudes mark some of the tops of the diapir structures between 80 and 100 km and in a depression at 110 km but without evidence for a BSR or bright spot (Figure 3).

4.2. *P* wave Velocity Analysis, Sediment Thickness, Velocity Anomalies

[23] Interval *P* wave velocity data are superimposed on the corresponding MCS profiles 01 and 02 (Figures 5–7). The interval velocities have been used to transfer the seismic data from the time to depth domain. Compressional wave velocities increase with depth from ~1500 to 2200 m/s (Figures 5–7).

4.2.1. On MCS Profile Line 01

[24] On MCS profile line 01, compressional wave velocities increase from 1500 m/s at the seabed to 2100 m/s in a localized region at the BSR between CMPs 11700 and 13500 (Figure 5). Velocities below the BSR are difficult to analyze because of indiscernible reflections (Figure 4). There is no possibility within the resolution of our seismic data for modeling the low-velocity free gas zone beneath the BSR. In comparison, velocities between CMPs 11200 and 16500 and between 17400 and 21500 on MCS profile line 02 also depict an increase in velocity from 1500 m/s at the seabed to 2200 m/s but in a more widespread area without a BSR (Figures 6 and 7). High velocities are also known to occur in debris flow deposits [e.g., *Plaza-Faverola et al.*, 2010]. Debris flows exist in the study area and extend toward the Knipovich Ridge.

4.2.2. On MCS Profile Line 02

[25] From ~110 km and toward the southeastern end of the line, the sediment thickness of GIII increases from about ~280 to ~820 m (Figure 3) on the basis of velocity modeling (Figure 7). The modeled seismic velocities of the GIII layer vary from 1500 m/s at ~70 km to 1900 m/s (Figures 6 and 7) at ~118 km toward the southeast along the seismic section (for location see Figure 3a). The GII sequence, which underlies the GIII sequence can be followed continuously from ~65 km to the end of the seismic line (Figure 3). Between ~65 km and ~125 km the sediment thickness of GII is influenced by the undulation of the

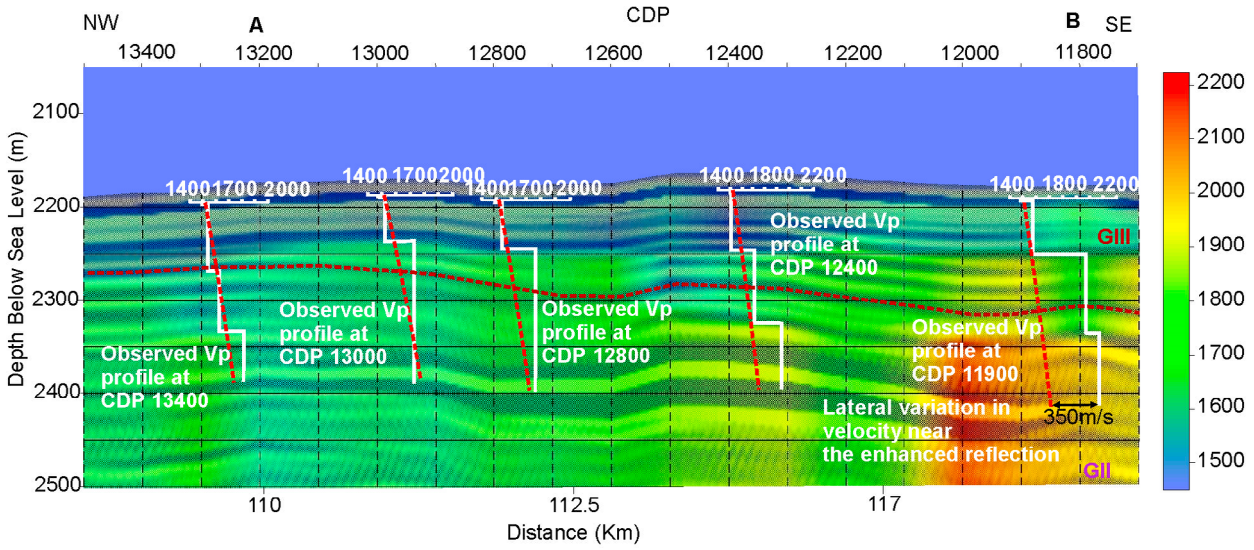

Figure 5. *P* wave velocity cross section derived from the MCS profile line 01 (see Figure 2a for location) superimposed on corresponding seismic section. Observed velocity profiles are shown as solid white lines, and the red dashed lines indicate the Hamilton reference velocity. High lateral variations in velocity (up to ~2100 m/s) above the BSR suggest partial saturation of gas hydrate. No velocity inversion can be found below the BSR because of indiscernible reflections. The area between points A and B shows the extension of the bright spot. Glacial sequences GIII (dark brown) and GII (purple) are marked on the seismic section.

underlying GI sequence and the thickness varies from 0 m at the pinch-out at the Knipovich Ridge to a maximum of ~210 m at 125 km (Figure 3). Southeastward of km 125, the GII thickness gradually increases to ~375 m at the end of the line. The modeled *P* wave velocity in the GII sequence increases from 1500 m/s at 70 km to 2100 m/s (Figures 6 and 7) at ~118 km along the seismic line (for location see Figure 3a).

[26] The undulating nature of the bounding layers induces also a variable sediment thickness of the GI sequence between 60 km and 115 km (Figure 3). From approximately 60 km to 105 km, the topography of this sequence changes with a few small highs in the interface and thickness varying between 100 m to 260 m. Farther southeastward and toward the end of the seismic line, the thickness gradually increases and varies between ~370 and ~860 m. The modeled

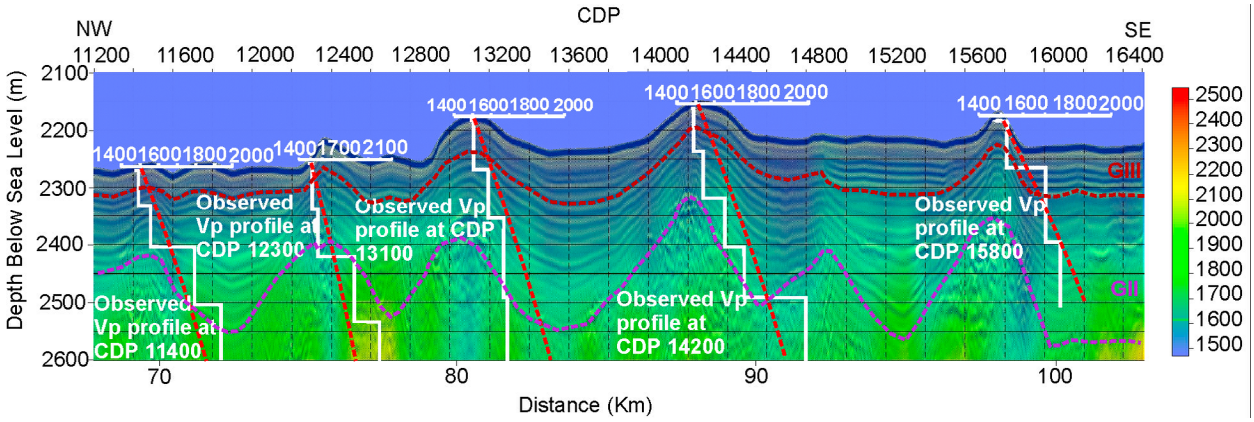

Figure 6. *P* wave velocity cross section derived from MCS profile line 02 (see Figure 3a for location) toward the Knipovich Ridge superimposed on the corresponding seismic section. Observed velocity profiles are shown as solid white lines, and the Hamilton reference velocity is shown as red dashed lines. High velocities (up to 2100 m/s) are observed and are interpreted to be caused by debris flows. The stratification pinch-out and the seabed are deformed by significant diapir-like structures. Glacial sequences GIII (dark brown) and GII (purple) are marked on the seismic section.

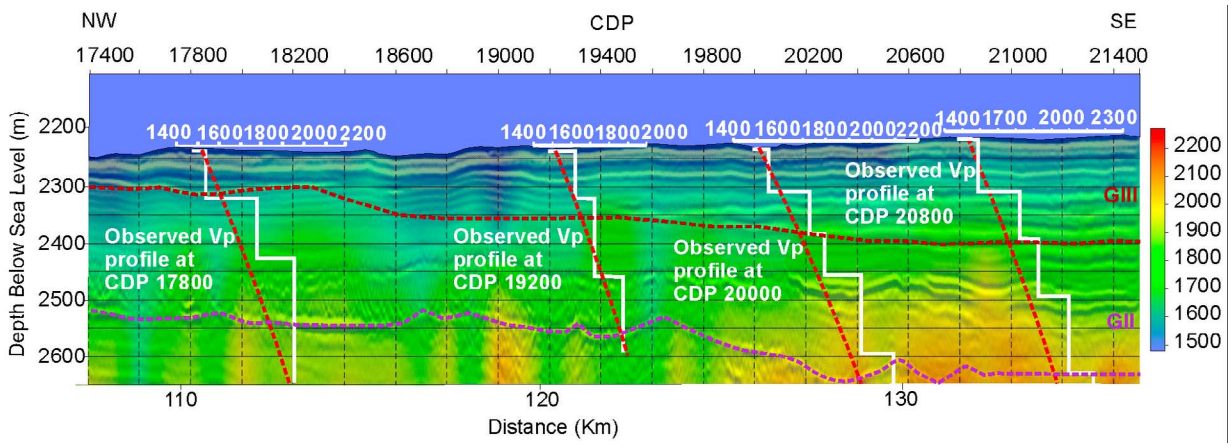

Figure 7. *P* wave velocity cross section derived from MCS profile line 02 (see Figure 3a for location) near the shelf edge superimposed on the corresponding seismic section. Observed velocities are shown as solid white lines, and the red dashed lines correspond to the Hamilton reference velocity. High velocities (up to 2200 m/s) are observed and are interpreted to be caused by debris flows. Glacial sequences GIII (dark brown) and GII (purple) are marked on the seismic section.

compressional wave velocity increases from 1900 m/s at 75 km to 2200 m/s at ~118 km (Figures 6 and 7) toward the southeast.

[27] The G0 sequence directly overlies oceanic basement and the topography of the basement influences the sedimentary thickness with notably reduced thicknesses at ~85 km and ~105 km along the seismic profile (Figure 3). The oceanic basement appears as a prominent reflection within the study area and is observed to extend from the eastern flank of the Knipovich Ridge to ~145 km. Chaotic seismic signatures characterize the G0 sequence and velocity modeling was deemed ineffectual because of this impediment.

4.3. Gas Hydrate Concentration

[28] The concentration of methane hydrate is predicted using the partial hydrate-cementing model [*Chand et al.*, 2006], under the assumption that the observed increases in *P* wave velocity above the BSR are anomalies related to the hydrate content within the pore space of sediments. Figure 8a shows the predicted methane hydrate saturation profile projected on the corresponding MCS profile line 01 (Figures 5 and 8).

[29] The prominent feature observed in the MCS profile line 01 shows the presence of a distinct BSR (Figure 4). It occurs between two buried diapirs and directly above the underlying crustal structures of the suggested serpentinized mantle and gabbro complex [*Kandilarov et al.*, 2008] (Figures 2a and 2b). The short BSR is suggested to represent the boundary between hydrate-bearing and gas-charged sediments beneath it. Modeling of the gas hydrate stability zone supports this interpretation with a theoretical BGHSZ at the depth of the observed BSR. The BGHSZ represents the present-day situation (Figure 8) where hydrates are generally stable above it. The model predicts methane hydrate concentrations of up to 26% of the pore space of sediments. A gas hydrate containing sediment layer may exists in a 60 to 240 m thick zone, which varies significantly because of possibly heterogeneous distribution of available gas, water, and/or pore space.

[30] The overall uncertainty of the hydrate modeling (Figure 8b) depends mainly on the use of a single sediment composition and the reference velocity depth profile for hydrate-free sediments. The velocity depth profile is derived from the smooth porosity-depth curve on the basis of data from ODP Leg 162 Site 986. We assumed 10% uncertainty for the porosity because of the changes in porosity at site 986 from the smooth porosity depth function [e.g., *Hustoft et al.*, 2009]. Since we use a broad interval velocity profile covering many layers, we assumed an uncertainty of 10% which could be considered as the highest level of uncertainty between the two picked vertical locations. The uncertainty in velocity will be reduced to picking uncertainty close to the picking locations which is less than 5%. The uncertainty in mineralogy is assumed to be 20% when comparing the variation in sediment types. These uncertainties are used to calculate the overall uncertainty during minimization within the inversion algorithm. Details of the methodology are given in *Chand et al.* [2006].

5. Discussion

5.1. Distribution of Gas Hydrate and/or Free Gas

[31] The Norwegian-Svalbard continental margin has a high potential for natural gas hydrate and several gas hydrate occurrences have been reported from these areas including sampling of gas hydrate [*Posewang and Mienert*, 1999; *Bünz and Mienert*, 2004; *Carcione et al.*, 2005; *Vanneste et al.*, 2005b; *Westbrook et al.*, 2005, 2008; *Hustoft et al.*, 2009].

[32] BSR occurrence in reflection seismic data has so far been the most important marker for the presence of gas hydrates in marine sediments. However, studies from a well known hydrate system at the Blake Ridge off the U.S. east coast shows that gas hydrate may occur without a BSR if free gas does not accumulate at the BGHSZ [*Holbrook*, 2001]. The fact that our studies show a bright spot (Figure 4) with the characteristics of a BSR, i.e., negative apparent polarity and strata crosscutting seismic events

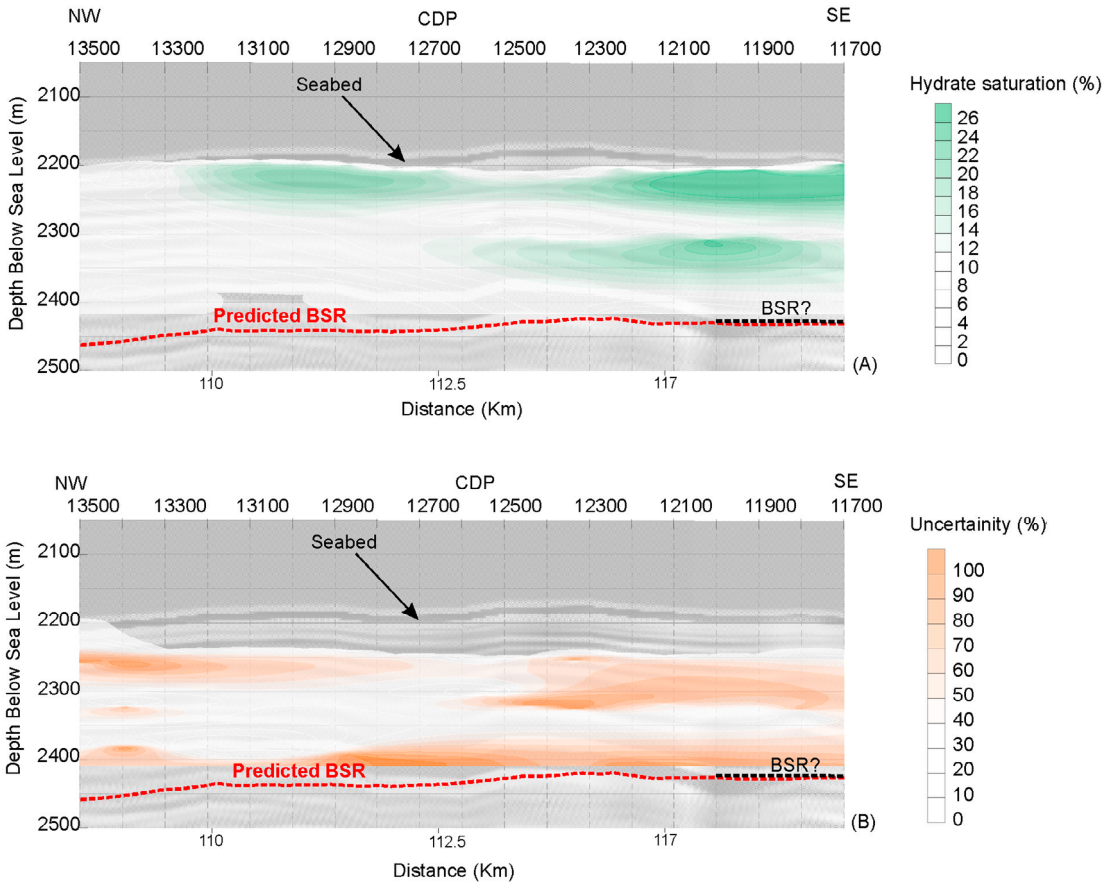

Figure 8. (a) Predicted methane hydrate saturation in the pore space of sediments with the corresponding MCS section line 01 superimposed. (b) Uncertainties in the estimation of the gas hydrate concentration due to the smooth porosity-depth model and single-sediment composition.

(Figure 4) indicate clearly the existence of gas hydrates within sediments close to the oceanic ridge. The BSR is predominantly the result of free gas trapped underneath the hydrate-bearing sediments. The appearance of a BSR is strongly related to the resolution of the seismic systems that influence the amplitudes at BSR depth [*Chapman et al.*, 2002; *Bünz and Mienert*, 2004]. The presence of gas hydrate/free gas north of Knipovich Ridge, at the Molløy Transform fault zone at NW Svalbard [*Vanneste et al.*, 2005b], is shown by a nearly continuous polarity reversed BSR created by up to 10% hydrate above and 3% of predicted free gas in the pore volume beneath it [*Vanneste et al.*, 2005b; *Hustoft et al.*, 2009]. The gas-rich layer varies in thickness with a minimum layer thickness of about 50m [*Vanneste et al.*, 2005b].

[33] Modeling of compressional wave velocities of the MCS data suggest the existence of gas hydrates on the eastern flank of Knipovich Ridge (Figure 8). Above the BSR, the deviation to the reference velocity (up to 350 m/s) and the magnitude of lateral velocity changes is significant and much greater than the estimated velocity uncertainty (Figure 5). If a heterogeneous facies distribution exists they may contribute to velocity changes as well. However, the significant positive velocity anomaly above the BSR is difficult to explain by changes in the lithologic composition of stratigraphic units, because the seismic data does not suggest lateral reflectivity changes along individual sequences (Figures 2a and 2b). The distinct increase in *P* wave velocity follows the BSR (Figure 5) as well as the predicted BGHSZ and suggests that it is related to this reflector. It is therefore reasonable to conclude that higher *P* wave velocities above the BSR document the presence of an appreciable amount of gas hydrates within the pore space of the sediments. The average concentration of gas hydrates is predicted to be up to 26% of the pore space of sediments with considerable variability and uncertainty in a 60 to 240 m thick zone that varies with depth significantly toward the BSR (Figure 8). Generally, the data reveals that BSRs, are prominent features north of the Knipovich Ridge but the sources of the gas are unclear. It is, however clear that free gas and gas hydrate form and accumulate in a sedimented area of an ultraslow oceanic rift system (Figures 2–3).

5.2. Occurrence of BSR and Enhanced Seismic Reflections Within Sequence Stratigraphic Units

[34] The thick sedimentary blanket covering the young oceanic crust was well resolved by tracing the three sedimentary sequences (Figures 2a and 3a).

[35] ODP site 986 results suggest that during the last ~1 Myr, the area has undergone more distal deposition and the main depocenters have shifted laterally. This has resulted in less frequent debris flows and more turbidities and

hemipelagic deposits, with a slight fining upward of the cored sediments. The results from the DSDP site 344 [*Talwani et al.*, 1976] supports a Pliocene age for the sequence G0 (Figures 1–3). A seismic line published by *Eiken and Hinz* [1993] (white solid line in Figure 1) correlates the borehole to the MCS profiles. A Pliocene age is suggested for the lowermost glacially influenced sediments, which is within the seismic sequence GI corresponding to SPI-II [*Schlüter and Hinz*, 1978]. The comparison of seismic lines along the SW Svalbard margin [*Vanneste et al.*, 2005b] (southern white square box in Figure 1) with the MCS profile line 01 illustrates also enhanced reflections, BSR like features and diapirs but at different sub bottom depth, elucidating the presence of gas.

5.3. Serpentinization at the Ultraslow Spreading Ridge and the Origin of Diapirism

[36] Interpretations of magnetic anomalies [*Engen et al.*, 2008] and spreading rates [*Kandilarov et al.*, 2008] have been integrated in the seismic profiles (Figures 1–3). The oceanic spreading rate based on profile line 01 between 80 and 130 km reaches ~5.5 mm/yr [*Kandilarov et al.*, 2008]. The ultraslow spreading rate at the ridges may generate a thin crust because of prolonged crustal stretching accompanied by thermal expansion. This period of thermal expansion may lead to circulation of seawater in the upper mantle which in turn can cause serpentinization [*Minshull et al.*, 1998; *Kandilarov et al.*, 2008].

[37] The serpentinization process as inferred [*Kandilarov et al.*, 2008, 2010] in the oceanic basement, led to a volumetric fluid increase. This volume increase might have mobilized sediments of the G0 and the GI sequence overlying the basement. Driven by overpressure and buoyancy the mobilized sediments move upward through the sedimentary column and this likely has resulted in the formation of the diapiric structures observed in the seismic data (Figures 2 and 3). These diapirs show a profound influence on the sedimentary sequences above GII-GIII at the ocean ridge over a distance of ~40 km between 70 and 110 km, which coincides with the inferred location of the serpentinized mantle (Figure 2) [*Kandilarov et al.*, 2008]. Elsewhere, similar structures have been interpreted as magmatic intrusions [*Lizarralde et al.*, 2011]. However, the structures that *Lizarralde et al.* [2011] present from the Guaymas spreading center show much higher acoustic impedance and scattering of seismic energy at their upper termination. The absence of these acoustics characteristics clearly distinguishes the diapirs at the Knipovich Ridge from the intrusions in the Guaymas basin.

[38] The degree of deformation due to the diapirism varies from structure to structure. The southeasternmost diapirs are buried features with adjacent reflections onlapping onto the flanks of diapirs (Figure 3). They show only a weak surface expression at the seafloor, which is likely due to differential compaction on top of the diapir compared to its bordering mini basins. Further northwest, the structures clearly deform recent sediments at the seafloor (Figures 2 and 3) and show variable degree of onlapping strata on their flanks (Figure 3), which indicates that sediment remobilization might have gone on over a long period of time. Furthermore, diapirism at the investigated areas appear to be an ongoing process as the serpentinization at the oceanic basement is assumed to occur over long time periods [*Kandilarov et al.*, 2008, 2010].

5.4. Mechanism for the Migration and Accumulation of Gas and Gas Hydrate

[39] Gas hydrate and free gas accumulates in a mini basin between two buried diapirs (Figures 2 and 4). Their spatial relationship with the diapirs suggests that their accumulation mechanism is related to the remobilization of sediments above the basement and the inferred region of serpentinized mantle [*Kandilarov et al.*, 2008]. Enhanced reflections occur beneath the diapiric structures almost all the way down to the basement indicating the presence of free gas. We consider that the bright spot and the enhanced reflections (Figures 2a–2c and 4) located adjacent to the diapirs and above the area of serpentinization may have been fed from deep sources of upward migrating gas. The source area lies in oceanic basement and is due to serpentinization (Figure 9). Slow spreading mid-ocean ridge segments may have elevated methane output because of serpentinization [e.g., *Bougault et al.*, 1993; *Charlou et al.*, 2010; *Kandilarov et al.*, 2010]. The heat that is produced during the serpentinization process might have resulted in an accelerated maturation of biogenic material, and might have also driven hydrocarbon to shallower strata where it would be consumed by hydrate formation. The deep hydrocarbon gases utilize the diapiric structures as migration pathways into shallow strata as indicated by the presence of gas within and adjacent to these structures. The fact that clear evidence for gas hydrates (Figures 4 and 5) exists only over a small area (Figure 2) is probably related to the availability/lack of suitable accommodation space. Suitable host rock exists only in the proximity of the two buried diapirs (Figure 2) where a sufficient amount of marine, possibly turbiditic sediments have accumulated. At this location, hydrocarbon gases, most likely mainly methane, have slowly accumulated and formed gas hydrates. The migration mechanism invoked herein suggests that gas hydrate could also occur shallower in the GHSZ, but the velocity data does not clearly indicate its presence elsewhere. That might be a consequence of the ongoing deformation of the seafloor and shallow subsurface by diapirism or due to the lack of sufficient amounts of hydrocarbon gases.

[40] Though the carbon release budget from young ocean spreading centers remains mainly unknown, the world mid-ocean ridge system may play a significant role in the release of carbon as exemplified by the sedimented ultraslow spreading Knipovich Ridge.

6. Conclusion

1. The suggested oceanic basement serpentinization causes methane release from deep sources and capture of methane in the shallow gas hydrate stability zone marked by a distinct BSR.

2. The sedimented ultraslow spreading Knipovich Ridge encompasses a deepwater methane hydrate reservoir. Significant *P* wave velocity variations above the BSR suggest average concentrations of gas hydrate up to 26% of the pore space of sediments in a 60 to 240 m thick zone which varies with depth significantly toward the BSR.

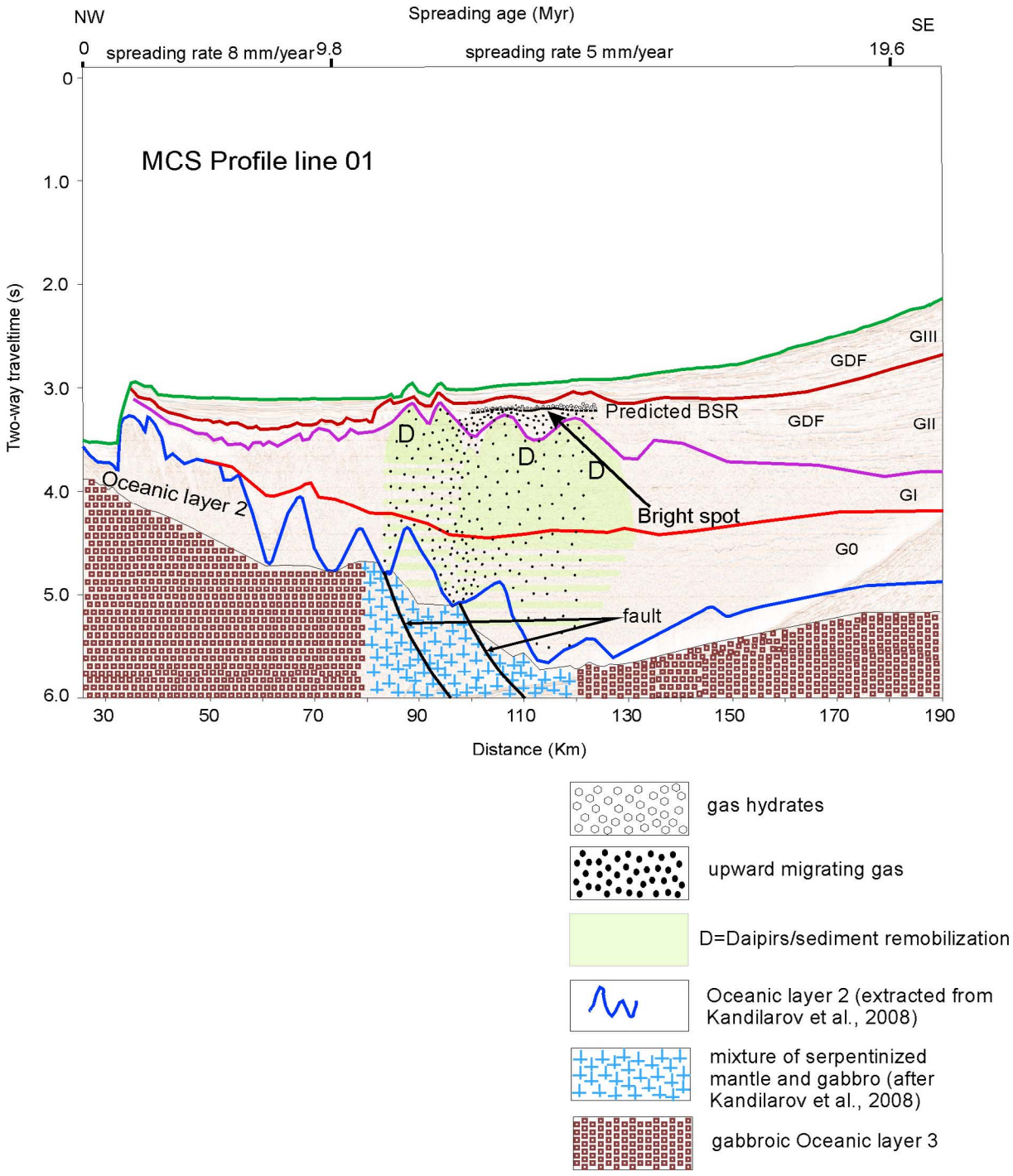

Figure 9. Schematic representation of oceanic layer 2, serpentinized mantle, and gabbro area (extracted from *Kandilarov et al.* [2008]), the potential pathways for upward migration of gas, and accumulation of gas within the gas hydrate stability zone at the upper glacial GII sediment sequence.

3. Diapirism occurs above regions of oceanic basement serpentinization adjacent to the Knipovich Ridge valley. Diapirs are characterized by chaotic seismic signatures, and some show enhanced seismic amplitudes on top. The features observed have led to the suggestion that the diapirs alter the chemistry of the sediments by their inherent thermal and pressure fields culminating in carbon release/migration.

4. Glacial sedimentary sequence GI – GIII and the preglacial sequence G0 drape the oceanic basement at the eastern side of the Knipovich Ridge. The southeastern area is controlled by glacial debris flows (GDF) that explain the location of high-interval *P* wave velocities. Sequences GIII and GII are glacial deposits with *P* wave velocities ranging between 1500 and 1900 m/s and 1500 and 2100 m/s,

respectively, while the seismic velocity in sequence GI (for profile 2) varies from 1900 to 2200 m/s.

[41] **Acknowledgments.** The authors acknowledge Rolf Mjelde from the University of Bergen for providing the MCS data. The University of Tromsø acknowledges support of this research project by Landmark Graphics Corporation via the Landmark University Grant Program. We are thankful to the University of Tromsø for financing the research project under the PhD program and to Tim Minshull (National Oceanography Centre, Southampton, UK) and Martin Hovland (Statoil) for providing helpful comments that improved the quality of the paper.

References

Bougault, H., J.-L. Charlou, Y. Fouquet, H. D. Needham, N. Vaslet, P. Appriou, P. J. Baptiste, P. A. Rona, L. Dmitriev, and S. Silantiev (1993), Fast and slow spreading ridges: Structure and hydrothermal activity, ultramafic topographic highs, and CH_4 output, *J. Geophys. Res.*, *98*(B6), 9643–9651, doi:10.1029/93JB00508.

Bünz, S., and J. Mienert (2004), Acoustic imaging of gas hydrate and free gas at the Storegga Slide, *J. Geophys. Res.*, *109*, B04102, doi:10.1029/2003JB002863.

Carcione, J. M., D. Gei, G. Rossi, and G. Madrussani (2005), Estimation of gas-hydrate concentration and free-gas saturation at the Norwegian-Svalbard continental margin, *Geophys. Prospect.*, *53*(6), 803–810, doi:10.1111/j.1365-2478.2005.00502.x.

Chand, S., T. A. Minshull, D. Gei, and J. M. Carcione (2004), Elastic velocity models for gas-hydrate-bearing sediments—A comparison, *Geophys. J. Int.*, *159*(2), 573–590, doi:10.1111/j.1365-246X.2004.02387.x.

Chand, S., T. A. Minshull, J. A. Priest, A. I. Best, C. R. I. Clayton, and W. F. Waite (2006), An effective medium inversion algorithm for gas hydrate quantification and its application to laboratory and borehole measurements of gas hydrate-bearing sediments, *Geophys. J. Int.*, *166*(2), 543–552, doi:10.1111/j.1365-246X.2006.03038.x.

Chand, S., J. Mienert, K. Andreassen, J. Knies, L. Plassen, and B. Fotland (2008), Gas hydrate stability zone modeling in areas of salt tectonics and pockmarks of the Barents Sea suggests an active hydrocarbon venting system, *Mar. Pet. Geol.*, *25*, 625–636, doi:10.1016/j.marpetgeo.2007.10.006.

Chapman, N. R., J. F. Gettrust, R. Walia, D. Hannay, G. D. Spence, W. T. Wood, and R. D. Hyndman (2002), High-resolution, deep-towed, multichannel seismic survey of deep-sea gas hydrates off western Canada, *Geophysics*, *67*(4), 1038–1047, doi:10.1190/1.1500364.

Charlou, J. L., J. P. Donval, C. Konn, H. Ondreas, Y. Fouquet, P. Jean-Baptiste, and E. Fourre (2010), High production and fluxes of H_2 and CH_4 and evidence of abiotic hydrocarbon synthesis by serpentinization in ultramafic-hosted hydrothermal systems on the Mid-Atlantic Ridge, in *Diversity of Hydrothermal Systems on Slow Spreading Ocean Ridges*, *Geophys. Monogr. Ser*, vol. 188, edited by P. Rona et al., pp. 265–296, AGU, Washington, D. C., doi:10.1029/2008GM000752.

Claypool, G. E., and K. A. Kvenvolden (1983), Methane and other hydrocarbon gases in marine sediment, *Annu. Rev. Earth Planet. Sci.*, *11*, 299–327, doi:10.1146/annurev.ea.11.050183.001503.

Crane, K., E. Sundvor, J. P. Foucher, M. Hobart, A. M. Myhre, and S. LeDouaran (1988), Thermal evolution of the western Svalbard margin, *Mar. Geophys. Res.*, *9*(2), 165–194, doi:10.1007/BF00369247.

Crane, K., E. Sundvor, R. Buck, and F. Martinez (1991), Rifting in the northern Norwegian-Greenland Sea: Thermal tests of asymmetric spreading, *J. Geophys. Res.*, *96*(B9), 14,529–14,550, doi:10.1029/91JB01231.

Crane, K., H. Doss, P. Vogt, E. Sundvor, G. Cherkashov, I. Poroshina, and D. Joseph (2001), The role of the Spitsbergen shear zone in determining morphology, segmentation and evolution of the Knipovich Ridge, *Mar. Geophys. Res.*, *22*(3), 153–205, doi:10.1023/A:1012288309435.

Dick, H. J. B., J. Lin, and H. Schouten (2003), An ultraslow-spreading class of ocean ridge, *Nature*, *426*(6965), 405–412, doi:10.1038/nature02128.

Dix, C. H. (1955), Seismic velocities from surface measurements, *Geophysics*, *20*, 68–86, doi:10.1190/1.1438126.

Ecker, C., J. Dvorkin, and A. M. Nur (2000), Estimating the amount of gas hydrate and free gas from marine seismic data, *Geophysics*, *65*(2), 565–573, doi:10.1190/1.1444752.

Eiken, O., and A. Austegard (1987), The Tertiary orogenic belt of West-Spitsbergen: Seismic expressions of the offshore sedimentary basins, *Nor. Geol. Tidsskr.*, *67*, 383–394.

Eiken, O., and K. Hinz (1993), Contourites in the Fram Strait, *Sediment. Geol.*, *82*(1–4), 15–32, doi:10.1016/0037-0738(93)90110-Q.

Engen, Ø., O. Eldholm, and H. Bungum (2003), The Arctic plate boundary, *J. Geophys. Res.*, *108*(B2), 2075, doi:10.1029/2002JB001809.

Engen, Ø., J. I. Faleide, and T. K. Dyreng (2008), Opening of the Fram Strait gateway: A review of plate tectonic constraints, *Tectonophysics*, *450*(1–4), 51–69, doi:10.1016/j.tecto.2008.01.002.

Faleide, J. I., A. Solheim, A. Fiedler, B. O. Hjelstuen, E. S. Andersen, and K. Vanneste (1996), Late Cenozoic evolution of the western Barents Sea-Svalbard continental margin, *Global Planet. Change*, *12*(1–4), 53–74, doi:10.1016/0921-8181(95)00012-7.

Fiedler, A., and J. I. Faleide (1996), Cenozoic sedimentation along the southwestern Barents Sea margin in relation to uplift and erosion of the shelf, *Global Planet. Change*, *12*(1–4), 75–93, doi:10.1016/0921-8181(95)00013-5.

Forsberg, C. F., A. Solheim, A. Elverhøi, E. Jansen, J. E. T. Channell, and E. S. Andersen (1999), The depositional environment of the western Svalbard margin during the late Pliocene and the Pleistocene: Sedimentary facies changes at site 986, *Proc. Ocean Drill. Program Sci. Results*, *162*, 233–246.

Früh-Green, G. L., D. S. Kelley, S. M. Bernasconi, J. A. Karson, K. A. Ludwig, D. A. Butterfield, C. Boschi, and G. Proskurowski (2003), 30,000 years of hydrothermal activity at the Lost City vent field, *Science*, *301*(5632), 495–498, doi:10.1126/science.1085582.

Hjelstuen, B. O., A. Elverhoi, and J. I. Faleide (1996), Cenozoic erosion and sediment yield in the drainage area of the Storfjorden Fan, *Global Planet. Change*, *12*(1–4), 95–117, doi:10.1016/0921-8181(95)00014-3.

Holbrook, W. S. (2001), Seismic studies of the Blake Ridge: Implications for hydrate distribution, methane expulsion, and free gas dynamics, in *Natural Gas Hydrates: Occurrence, Distribution, and Detection*, *Geophys. Monogr. Ser*, vol. 124, edited by C. K. Paull and W. P. Dillon, pp. 235–256, AGU, Washington, D. C., doi:10.1029/GM124p0235.

Holbrook, W. S., H. Hoskins, W. T. Wood, R. A. Stephen, and D. Lizarralde (1996), Methane hydrate and free gas on the Blake Ridge from vertical seismic profiling, *Science*, *273*(5283), 1840–1843, doi:10.1126/science.273.5283.1840.

Holbrook, W. S., D. Lizarralde, I. A. Pecher, A. R. Gorman, K. L. Hackwith, M. Hornbach, and D. Saffer (2002), Escape of methane gas through sediment waves in a large methane hydrate province, *Geology*, *30*(5), 467–470, doi:10.1130/0091-7613(2002)030<0467:EOMGTS>2.0.CO;2.

Hustoft, S., S. Bünz, J. Mienert, and S. Chand (2009), Gas hydrate reservoir and active methane-venting province in sediments on <20 Ma young oceanic crust in the Fram Strait, offshore NW-Svalbard, *Earth Planet. Sci. Lett.*, *284*(1–2), 12–24, doi:10.1016/j.epsl.2009.03.038.

Hydratech (2004), Quantitative estimates of hydrate and free gas saturation in the representative seismic survey areas, *Final Rep. Annex 15*, Birmingham, U. K.

Hyndman, R. D., and G. D. Spence (1992), A seismic study of methane hydrate marine bottom simulating reflectors, *J. Geophys. Res.*, *97*(B5), 6683–6698, doi:10.1029/92JB00234.

Jakobsen, M., J. A. Hudson, T. A. Minshull, and S. C. Singh (2000), Elastic properties of hydrate-bearing sediments using effective medium theory, *J. Geophys. Res.*, *105*(B1), 561–577, doi:10.1029/1999JB900190.

Jakobsson, M., N. Cherkis, J. Woodward, B. J. Coakley, and R. Macnab (2000), A new grid of Arctic bathymetry: A significant resource for scientists and map makers, *Eos Trans. AGU*, *81*(9), 89, doi:10.1029/00EO00059.

Judd, A. G., and M. Hovland (2007), *Seabed Fluid Flow: The Impact on Geology, Biology, and the Marine Environments*, 475 pp., Cambridge Univ. Press, New York.

Judd, A. G., M. Hovland, L. I. Dimitrov, S. García Gil, and V. Jukes (2002), The geological methane budget at continental margins and its influence on climate change, *Geofluids*, *2*(2), 109–126, doi:10.1046/j.1468-8123.2002.00027.x.

Kandilarov, A., R. Mjelde, K. Okino, and Y. Murai (2008), Crustal structure of the ultra-slow spreading Knipovich Ridge, North Atlantic, along a presumed amagmatic portion of oceanic crustal formation, *Mar. Geophys. Res.*, *29*(2), 109–134, doi:10.1007/s11001-008-9050-0.

Kandilarov, A., H. Landa, R. Mjelde, R. B. Pedersen, K. Okino, and Y. Murai (2010), Crustal structure of the ultra-slow spreading Knipovich Ridge, North Atlantic, along a presumed ridge segment center, *Mar. Geophys. Res.*, *31*, 173–195, doi:10.1007/s11001-010-9095-8.

Kelley, D. S., and G. L. Früh-Green (1999), Abiogenic methane in deep-seated mid-ocean ridge environments: Insights from stable isotope analyses, *J. Geophys. Res.*, *104*(B5), 10,439–10,460, doi:10.1029/1999JB900058.

Kelley, D. S., et al. (2005), A serpentinite-hosted ecosystem: The Lost City hydrothermal field, *Science*, *307*(5714), 1428–1434, doi:10.1126/science.1102556.

Kvenvolden, K. A. (1988), Methane hydrate—A major reservoir of carbon in the shallow geosphere?, *Chem. Geol.*, *71*(1–3), 41–51, doi:10.1016/0009-2541(88)90104-0.

Lizarralde, D., S. A. Soule, J. S. Seewald, and G. Proskurowski (2011), Carbon release by off-axis magmatism in a young sedimented spreading centre, *Nat. Geosci.*, *4*(1), 50–54, doi:10.1038/ngeo1006.

Ljones, F., A. Kuwano, R. Mjelde, A. Breivik, H. Shimamura, Y. Murai, and Y. Nishimura (2004), Crustal transect from the North Atlantic

Knipovich Ridge to the Svalbard margin west of Hornsund, *Tectonophysics*, *378*(1–2), 17–41, doi:10.1016/j.tecto.2003.10.003.

Lundin, E., and A. G. Doré (2002), Mid-Cenozoic post-breakup deformation in the 'passive' margins bordering the Norwegian-Greenland Sea, *Mar. Pet. Geol.*, *19*(1), 79–93, doi:10.1016/S0264-8172(01)00046-0.

Markl, R. G., G. M. Bryan, and J. I. Ewing (1970), Structure of the Blake-Bahama Outer Ridge, *J. Geophys. Res.*, *75*(24), 4539–4555, doi:10.1029/JC075i024p04539.

Mienert, J., et al. (2001), Western Svalbard continental margin–gas hydrates, R/V *Jan Mayen* Hydratech cruise report, 124 pp., Dep. of Geol., Univ. of Tromsø, Tromsø, Norway.

Minshull, T. A., M. R. Muller, C. J. Robinson, R. S. White, and M. J. Bickle (1998), Is the oceanic Moho a serpentinization front?, *Geol. Soc. Spec. Publ.*, *148*(1), 71–80, doi:10.1144/GSL.SP.1998.148.01.05.

Mosar, J., E. A. Eide, P. T. Osmundsen, A. Sommaruga, and T. H. Torsvik (2002), Greenland-Norway separation: A geodynamic model for the North Atlantic, *Nor. J. Geol.*, *82*, 281–298.

Myhre, A. M. (1984), Compilation of seismic velocity measurements along the margins of the Norwegian-Greenland Sea, *Nor. Polarinst. Skr.*, *180*, 41–61.

Myhre, A. M., and O. Eldholm (1988), The western Svalbard margin (74°–80°N), *Mar. Pet. Geol.*, *5*(2), 134–156, doi:10.1016/0264-8172(88)90019-0.

Myhre, A. M., O. Eldholm, and E. Sundvor (1982), The margin between Senja and Spitsbergen fracture zones: Implications from plate tectonics, *Tectonophysics*, *89*(1–3), 33–50, doi:10.1016/0040-1951(82)90033-6.

Okino, K., D. Curewitz, M. Asada, K. Tamaki, P. Vogt, and K. Crane (2002), Preliminary analysis of the Knipovich Ridge segmentation: Influence of focused magmatism and ridge obliquity on an ultraslow spreading system, *Earth Planet. Sci. Lett.*, *202*(2), 275–288, doi:10.1016/S0012-821X(02)00790-2.

Planke, S. (1989), *HEAT—A Heat Flow Database Program*, Mar. and Appl. Geophys. Res. Group, Dep. of Geol., Univ. of Oslo, Oslo.

Plaza-Faverola, A., S. Bünz, and J. Mienert (2010), Fluid distributions inferred from *P* wave velocity and reflection seismic amplitude anomalies beneath the Nyegga pockmark field of the mid-Norwegian margin, *Mar. Pet. Geol.*, *27*(1), 46–60, doi:10.1016/j.marpetgeo.2009.07.007.

Posewang, J., and J. Mienert (1999), The enigma of double BSRs: Indicators for changes in the hydrate stability field?, *Geo Mar. Lett.*, *19*(1–2), 157–163, doi:10.1007/s003670050103.

Proskurowski, G., M. D. Lilley, J. S. Seewald, G. L. Früh-Green, E. J. Olson, J. E. Lupton, S. P. Sylva, and D. S. Kelley (2008), Abiogenic hydrocarbon production at Lost City hydrothermal field, *Science*, *319*(5863), 604–607, doi:10.1126/science.1151194.

Ritzmann, O., W. Jokat, R. Mjelde, and H. Shimamura (2002), Crustal structure between the Knipovich Ridge and the Van Mijenfjorden (Svalbard), *Mar. Geophys. Res.*, *23*(5/6), 379–401, doi:10.1023/B:MARI.0000018168.89762.a4.

Ritzmann, O., W. Jokat, W. Czuba, A. Guterch, R. Mjelde, and Y. Nishimura (2004), A deep seismic transect from Hovgård Ridge to northwestern Svalbard across the continental-ocean transition: A sheared margin study, *Geophys. J. Int.*, *157*(2), 683–702, doi:10.1111/j.1365-246X.2004.02204.x.

Sarkar, S., C. Berndt, A. Chabert, D. G. Masson, T. A. Minshull, and G. K. Westbrook (2011), Switching of a paleo-ice stream in northwest Svalbard, *Quat. Sci. Rev.*, *30*(13–14), 1710–1725, doi:10.1016/j.quascirev.2011.03.013.

Schlüter, H. U., and K. Hinz (1978), The continental margin of West-Spitsbergen, *Polarforschung*, *48*, 151–169.

Shipboard Scientific Party (1996), Site 986, *Proc. Ocean Drill. Program Initial Rep.*, *162*, 287–342.

Shipley, T. H., M. H. Houston, R. T. Buffler, F. J. Shaub, K. J. McMillen, J. W. Ladd, and J. L. Worzel (1979), Seismic evidence for widespread possible gas hydrate horizons on continental slopes and rises, *AAPG Bull.*, *63*(12), 2204–2213.

Sleep, N. H., A. Meibom, T. Fridriksson, R. G. Coleman, and D. K. Bird (2004), H_2-rich fluids from serpentinization: Geochemical and biotic implications, *Proc. Natl. Acad. Sci. U. S. A.*, *101*(35), 12,818–12,823, doi:10.1073/pnas.0405289101.

Sloan, E. D., Jr. (1998), Gas hydrates: Review of physical/chemical properties, *Energy Fuels*, *12*(2), 191–196, doi:10.1021/ef970164+.

Stolt, T. H. (1978), Migration by Fourier transform, *Geophysics*, *43*, 23–48, doi:10.1190/1.1440826.

Sundvor, E., and O. Eldholm (1979), The western and northern margin off Svalbard, *Tectonophysics*, *59*(1–4), 239–250, doi:10.1016/0040-1951(79)90048-9.

Sundvor, E., O. Eldholm, T. P. Gladczenko, and S. Planke (2000), Norwegian-Greenland Sea thermal field, *Geol. Soc. Spec. Publ.*, *167*(1), 397–410, doi:10.1144/GSL.SP.2000.167.01.15.

Talwani, M., and O. Eldholm (1977), Evolution of the Norwegian-Greenland Sea, *Geol. Soc. Am. Bull.*, *88*(7), 969–999, doi:10.1130/0016-7606(1977)88<969:EOTNS>2.0.CO;2.

Talwani, M., et al. (1976), Site 344, *Initial Rep. Deep Sea Drill. Proj.*, *38*, 389–449.

Vance, S., J. Harnmeijer, J. Kimura, H. Hussmann, B. Demartin, and J. M. Brown (2007), Hydrothermal systems in small ocean planets, *Astrobiology*, *7*(6), 987–1005, doi:10.1089/ast.2007.0075.

Vanneste, M., S. Guidard, and J. Mienert (2005a), Bottom-simulating reflections and geothermal gradients across the western Svalbard margin, *Terra Nova*, *17*(6), 510–516, doi:10.1111/j.1365-3121.2005a.00643.x.

Vanneste, M., S. Guidard, and J. Mienert (2005b), Arctic gas hydrate provinces along the western Svalbard continental margin, *Norw. Pet. Soc. Spec. Publ.*, *12*, 271–284.

Westbrook, G. K., et al. (2005), Measurement of *P*- and *S*-wave velocities and the estimation of hydrate concentration at sites in the continental margin of Svalbard and the Storegga region of Norway, in *Proceedings of Fifth International Conference on Gas Hydrates*, pp. 726–735, Curran Assoc., Red Hook, N. Y.

Westbrook, G. K., et al. (2008), Estimation of gas hydrate concentration from multi-component seismic data at sites on the continental margins of NW Svalbard and the Storegga region of Norway, *Mar. Pet. Geol.*, *25*(8), 744–758, doi:10.1016/j.marpetgeo.2008.02.003.

Westbrook, G. K., et al. (2009), Escape of methane gas from the seabed along the West Spitsbergen continental margin, *Geophys. Res. Lett.*, *36*(15), L15608, doi:10.1029/2009GL039191.

Yamano, M., S. Uyeda, Y. Aoki, and T. H. Shipley (1982), Estimates of heat flow derived from gas hydrates, *Geology*, *10*(7), 339–343, doi:10.1130/0091-7613(1982)10<339:EOHFDF>2.0.CO;2.

Yilmaz, O. (1987), *Seismic Data Processing: Investigation in Geophysics*, Soc. of Explor. Geophys., Tulsa, Okla.

S. Bünz, J. Mienert, and A. Rajan, Department of Geology, University of Tromsø, Dramsveien-201, N-9037 Tromsø, Norway. (stefan.buenz@uit.no; jurgen.mienert@uit.no; anupama.rajan@uit.no)

S. Chand, Geological Survey of Norway, PO Box 6315 Sluppen, N-7491 Trondheim, Norway. (shyam.chand@ngu.no)